



Efficient low-loaded ternary Pd-In₂O₃-Al₂O₃ catalysts for methanol production

Nicola Schiaroli^a, Leila Negahdar^{b,c}, Mads Lützen^d, Phuoc Hoang Ho^e, Lisa J. Allen^{b,c}, Alejandro Natoli^{a,f}, Francesca Ospitali^a, Francesco Maluta^{a,f}, Enrique Rodríguez-Castellón^g, Christian D. Damsgaard^{d,h}, Giuseppe Fornasari^{a,f}, Andrew M. Beale^{b,c,*}, Patricia Benito^{a,f,*}

^a Dipartimento di Chimica Industriale "Toso Montanari", Alma Mater Studiorum – Università di Bologna, Viale Risorgimento 4, 40136, Bologna, Italy

^b Chemistry Department, University College of London, Gordon Street, London, WC1H 0AJ, UK

^c UK Catalysis Hub, Research Complex at Harwell, Rutherford Appleton Laboratory, Didcot, OX110FA, UK

^d National Centre for Nano Fabrication and Characterization, Technical University of Denmark, Fysikvej Building 307, 2800 Kgs. Lyngby, Denmark

^e Chemical Engineering, Competence Centre for Catalysis, Chalmers University of Technology, SE-41296 Gothenburg, Sweden

^f Center for Chemical Catalysis – C3, Alma Mater Studiorum – Università di Bologna, Viale Risorgimento 4, 40136, Bologna, Italy

^g Universidad de Málaga, Departamento de Química Inorgánica, Facultad de Ciencias. 29071 Málaga, Spain

^h Department of Physics, Technical University of Denmark, Fysikvej Building 311, 2800 Kgs. Lyngby, Denmark

ARTICLE INFO

Article history:

Received 29 January 2023

Revised 15 April 2023

Accepted 7 May 2023

Available online 16 May 2023

Keywords:

Indium

Alumina

Methanol

Coprecipitation

In situ characterization

ABSTRACT

Pd-In₂O₃ catalysts are among the most promising alternatives to Cu-ZnO-Al₂O₃ for synthesis of CH₃OH from CO₂. However, the intrinsic activity and stability of In₂O₃ per unit mass should be increased to reduce the content of this scarcely available element and to enhance the catalyst lifetime. Herein, we propose and demonstrate a strategy for obtaining highly dispersed Pd and In₂O₃ nanoparticles onto an Al₂O₃ matrix by a one-step coprecipitation followed by calcination and activation. The activity of this catalyst is comparable with that of a Pd-In₂O₃ catalyst (0.52 vs 0.55 g_{MeOH} h⁻¹ g_{cat}⁻¹ at 300 °C, 30 bar, 40,800 mL h⁻¹ g_{cat}⁻¹) but the In₂O₃ loading decreases from 98 to 12 wt% while improving the long-term stability by three-fold at 30 bar. In the new Pd-In₂O₃-Al₂O₃ system, the intrinsic activity of In₂O₃ is highly increased both in terms of STY normalized to In specific surface area and In₂O₃ mass (4.32 vs 0.56 g_{MeOH} h⁻¹ g_{In2O3}⁻¹ of a Pd-In₂O₃ catalyst operating at 300 °C, 30 bar, 40,800 mL h⁻¹ g_{cat}⁻¹). The combination of *ex situ* and *in situ* catalyst characterizations during reduction provides insights into the interaction between Pd and In and with the support. The enhanced activity is likely related to the close proximity of Pd and In₂O₃, wherein the H₂ splitting activity of Pd promotes, in combination with CO₂ activation over highly dispersed In₂O₃ particles, facile formation of CH₃OH.

© 2023 The Authors. Published by Elsevier Inc. This is an open access article under the CC BY license (<http://creativecommons.org/licenses/by/4.0/>).

1. Introduction

The production of green methanol via the CO₂ thermocatalytic hydrogenation is a challenging process due to thermodynamic and kinetic issues [1]. The catalyst plays an important role and controls the activity and selectivity of the process. Several attempts have been made to replace the conventional Cu-ZnO-Al₂O₃ catalyst since the high-water content produced in the reaction leads to sintering of copper and thereby catalyst deactivation [2,3]. Among the different alternatives, In₂O₃-based catalysts are the most promising due to their superior methanol selectivity even at high temperature (300 °C) [4]. The ability of In₂O₃ to activate both CO₂ and H₂ in oxygen vacancies was initially predicted by DFT [5] and later it

was experimentally confirmed [6–9]. Since then, the performance of In-based catalysts has been improved, following the two most common approaches in catalysis: promotion with a metal and dispersion on a support [4].

The presence of Pd provides metallic sites for the H₂ dissociative adsorption and interfacial sites for CO₂ adsorption and hydrogenation [10]. Pd promotion is certainly effective, i.e. PdIn₂O₃ has been shown to be a more active catalyst than In₂O₃/ZrO₂ [11], although Pd activates the reverse water gas shift (RWGS). Moreover, PdIn intermetallics could be developed by treating in H₂ Pd/In₂O₃ catalysts [12,13] or during reaction [14]. The PdIn intermetallics are reported to have two opposite effects on the catalytic performance. Ye et al. stated that the PdIn intermetallic reduces the activity toward H₂ dissociative adsorption, weakens CO binding on the surface and increases the barrier of CO hydrogenation, suppressing

* Corresponding authors.

further hydrogenation beyond CO [15]. To overcome this issue, the Pd-support interaction is reduced by depositing preformed Pd⁰ particles [16] or by anchoring low nuclearity Pd clusters to the In₂O₃ matrix by controlled co-precipitation [17]. On the other hand, in the liquid phase CO₂ hydrogenation, unsupported PdIn nanoparticles show high activity, outperforming the conventional Cu/ZnO/Al₂O₃ catalyst [18]. Similarly, Snider et al. report an increase in activity for PdIn/SiO₂ [19]; the synergy between In₂O₃ and PdIn particles, which are surface In enriched, maximizes the methanol synthesis.

The contrasting observations could be related to the composition of PdIn particles [20,21], demonstrated to alter the activity in the methanol steam reforming, [12,22]. Moreover, the selectivity may be modified with the Pd particle size and pressure [23]. An increase in the particle size of Pd deposited on In₂O₃ favors the RWGS [17]. Another aspect likely involved in the activity of Pd-In₂O₃ catalysts is the reduction of In₂O₃ to In⁰ [24]. This depends on the reaction temperature and the selectivity of the process, and, more significantly, under experimental conditions, the reduction of In₂O₃ may not be homogeneous through the catalyst [25]. Hence, the catalyst is a mixture of In₂O₃ and In⁰, and its bulk characterization may not provide accurate information about the actual active sites. Moreover, the morphology of In₂O₃ can modify both the Pd electronic properties and the strong metal-support interaction (SMSI) between Pd and In₂O₃ [26].

In₂O₃ sintering, induced by H₂ [8], is delayed by deposition on ZrO₂ [8,11,27,28]. However, the role of the support is more complex than the simple In₂O₃ dispersion and formation of smaller crystallites [8] and notably, it depends on the ZrO₂ crystalline phase [29]. ZrO₂ contributes to the CO₂ activation, [27] modifies the In₂O₃ reducibility, and in turn the number of vacancies (active sites), as well as the In₂O₃ electronic properties [25,27,28]. Electron transfer from monoclinic ZrO₂ to In₂O₃ improves the electron density of In₂O₃, which promotes H₂ dissociation and hydrogenation of the formate intermediate to methanol [29]. Less attention has been paid to the use of Al₂O₃ as a support, despite it being reported that In₂O₃ can be easily dispersed on γ -Al₂O₃ [30], increasing the amount of highly dispersed In₂O₃ in comparison to ZrO₂ and SiO₂ (In₂O₃/Al₂O₃ > In₂O₃/ZrO₂ >> In₂O₃/SiO₂) [31]. This can be related to the poor activity of In₂O₃-Al₂O₃ systems in the CO₂ conversion to CH₃OH [8,11,27]. Conversely, the incorporation of Rh in the mixed oxide improves the activity [32]. A RhIn/Al₂O₃ catalyst (Rh 5 wt% and In/Al = 1/1) effectively catalyzes methanol synthesis and inhibits the RWGS under H₂-deficient gas flow; the activity being related to the strong synergy between Rh and In, specifically to bimetallic RhIn particles. However, both Rh and In loadings are high, indeed the authors suggest that some efforts need to be devoted to decrease both Rh and In loading.

Herein, an easy and simple approach is adopted to further develop CH₃OH synthesis catalysts, where Al₂O₃ is chosen to disperse low amounts of Pd and In₂O₃, considering the availability and price of In and Pd. The aim of this work is to establish the basis to develop Pd-In enhanced catalysts for methanol production, not only in terms of activity and stability, but also in economic feasibility, as well as operational flexibility during transient processes. Here we show that the combination of inactive bulk Pd-Al₂O₃ and In₂O₃-Al₂O₃ catalysts, with optimized-yet-low Pd and In₂O₃ loadings, produces a catalyst that is capable of reaching a space time yield (STY) close to that of Pd-In₂O₃ catalyst, but with considerable improvement in stability with time on stream. To understand the Pd and In species interaction in the performance, the catalysts have been studied using *ex situ* and *in situ* characterization techniques including X-ray photoelectron spectroscopy (XPS), X-ray absorption spectroscopy (XAFS), X-ray diffraction (XRD), N₂ physisorption, CO chemisorption, transmission electron microscopy (TEM), H₂-TPR and CO₂-TPD.

2. Experimental section

2.1. Preparation and characterization of the catalysts

The catalysts were prepared by co-precipitation followed by calcination. PdCl₂ (Sigma Aldrich, 99 %) was first dissolved in 10 mL of deionized water with the addition of some drops of HCl (Merck, 37 %) under stirring. This solution was added to an Al(NO₃)₃·9H₂O and/or In(NO₃)₃·5H₂O (Sigma Aldrich) aqueous solution under stirring at room temperature to give a 0.2 M solution with the appropriate cation molar ratios to obtain a final Pd loading of 1 or 0.5 wt% and an In₂O₃ content of 6, 12 or 23 wt% in the catalyst. A Na₂CO₃ aqueous solution (10 wt%) was added dropwise to the solution of the metals under stirring at room temperature until a pH of 9.2 was reached. After aging the slurry for 1 h, the precipitate was recovered by filtration, washed with deionized water and dried at 50 °C overnight. From the ICP analyses of the mother liquor the total precipitation of Pd, In and Al was confirmed. The obtained Pd/In/Al hydroxide precursors were calcined at 500 °C for 6 h (heating rate, 10 °C/min) and the catalyst composition was confirmed by EDS analyses. The catalysts were named Pd-6In₂O₃-Al₂O₃, Pd-12In₂O₃-Al₂O₃, Pd-23In₂O₃-Al₂O₃, and 0.5Pd-12In₂O₃-Al₂O₃, where 6, 12, and 23 referred to the In₂O₃ wt%. Two weight loadings of Pd were used: 0.5 and 1 %. Only the samples containing 0.5 Pd wt.% are specifically indicated whereas samples without a number before Pd contain 1 wt%. For comparison purposes, Pd-Al₂O₃, Pd-In₂O₃ with 1 Pd wt.%, and In₂O₃ catalysts were prepared following the same procedure as for the mixed oxides, the only difference is that for Pd-In₂O₃ and In₂O₃ the precursors are calcined at 300 °C to prevent excessive loss of active surface.

XRD powder analyses were carried out using a PANalytical X'Pert diffractometer equipped with a copper anode (Cu K α , λ = 0.15148 nm) and a fast X'Celerator detector. A 2 θ range from 5 to 80° was investigated, using a step size of 0.05° and scan step time of 15.25 s. The average In₂O₃ crystallite sizes in Pd-In₂O₃ catalysts were determined from the full width at half maximum (FWHM) of the In₂O₃ (222) XRD peak using the Scherrer formula.

The reduction profiles of the catalysts were obtained by H₂ temperature-programmed reduction (H₂-TPR) using a Micromeritics AutoChem II Chemisorption Analyzer equipped with a Thermal Conductivity Detector (TCD). After the pretreatment of the catalyst (ca. 150 mg) at 150 °C under 30 mL min⁻¹ of He for 1 h, the sample was cooled at -10 °C (using a Cryocooler system). The reduction was carried out by switching the carrier gas to 5 % H₂/Ar (v/v) at 30 mL min⁻¹. After the stabilization of the baseline, the temperature was increased to 900 °C (10 °C/min) and kept for 30 min.

X-ray Absorption Spectroscopy (XAS) measurements were conducted at the B18 beamline of the Diamond Light Source (DLS), UK. XAS measurements were performed at the Pd and In K-edge in transmission mode using the quick EXAFS (QEXAFS) setup with a fast-scanning Si (311) double crystal monochromator [33]. The data acquisition setup consisted of three detectors measuring the incident beam intensity, I₀, the transmitted beam through the sample, I_t, and the one through the reference, I_{ref}. A standard Pd or In foil reference was placed between I_t and I_{ref} and each spectrum was acquired with an exposure time of 180 s. The X-ray beam size was optimised to around 200 μ m \times 100 μ m for the measurement through the narrow X-ray access slits of the capillary reactor, which was placed on an adjustable stage in order to allow the alignment of the beam inside the X-ray slits.

For *in situ* measurements the catalyst particles (25 mg of 53–63 μ m sieve fraction) were loaded into the capillary reactor. The catalyst was heated up at 10 °C min⁻¹ under 10 % O₂/He flow and calcined at 400 °C for 60 min. The temperature was kept at

400 °C and the gas flow was switched from 10 % O₂/He to H₂ with a flow rate of 40 NmLmin⁻¹. For *ex situ* measurements, catalyst samples of reduced and post-reaction were solid pellets, prepared by mixing the material with cellulose filler.

The raw XAS spectra were processed using Athena/Artemis software [34]. The X-ray absorption near edge structure (XANES) spectra were pre-edge subtracted and normalised to the post edge background. The linear combination fitting (LCF) of the normalised XANES spectra was then performed around the Pd K-edge, 24150–24986 eV, using Athena software. The XANES spectra of the reference Pd metal foil were used as standard for the palladium metal (Pd⁰) in the LCF, while for the PdO component the spectra at the inlet during calcination were taken as reference. Their weightings were constrained to be between 0 and 1 and their sum to be equal to 1. The fitting quality was assessed using R-factors, which were consistently low for all the fittings. The Fourier transform (FT) of the EXAFS data was performed on the *k*³-weighted functions between 2.7 and 10 Å⁻¹. The following information was used for fitting of the Pd data: *S*0² = 0.83, *K*-range = 1.9 – 8.5 Å⁻¹ and an *R* range = 1 – 3.5 Å.

The other techniques used to characterize the catalysts at the different steps of their lifetime are detailed in [Supporting Information \(SI\)](#).

2.2. Catalytic tests

The calcined catalysts were pressed at 10 Ton for 20 min to produce a tablet, crushed and sieved to obtain particles with a dimension in the range of 30–40 mesh (0.595–0.400 mm). 0.5 g of the solids were then mixed with SiC (30–40 mesh) to reach a total volume of 1.2 cm³. The sample was placed between two layers of inert material (quartz) in a tubular reactor (INCOLOY 800HT) with an internal diameter of 10 mm and vertically placed into an electric tubular furnace. The gas flow rates were controlled by thermal mass flow controllers (Brooks Instruments), the operating pressure was set by a back-pressure regulator (Swagelok), and all the lines after the reactor outlet were heated at 200 °C to prevent condensation of methanol and water. Before tests, the reduction of the catalysts was performed *in situ*, flowing a mixture of H₂/N₂ (1/3 v/v, 120 mL min⁻¹), increasing the oven temperature from 50 to 300 °C (1 °C min⁻¹) and holding this temperature for 2 h. CO₂ hydrogenation to methanol was conducted by feeding a mixture of H₂, CO₂ and CH₄ (used as internal standard [17]) a H₂/CO₂/CH₄ ratio of 3/1/0.67, 4/1/0.67, or 5/1/0.67 (v/v). Catalytic tests were carried out at 20 or 30 bar and GHSV values in the range of 14,400 – 48,000 mL/g_{cat}h. In a typical test, the reactor was purged with N₂ until 175 °C and then pressurized to the working pressure

using the reaction mixture. The activity of the catalysts was monitored at an increasing temperature from 175 to 300 °C. The stability tests on the activated catalysts at high time-on-stream (TOS) were performed after these series of tests (8 h of TOS), reaching up to 100 h of TOS at 280 °C and 300 °C with several shut down cycles carried out by depressurizing the reactor and maintaining the catalyst under N₂ at the working temperature overnight. The reaction stream was analysed by an online gas chromatograph (Agilent Technology 7890A) equipped with two thermal conductivity detectors (TCD) and a CarboPLOT P7 column using H₂ for the CH₄, CO, CO₂, CH₃OH analyses and an HP-Molesieve column using N₂ for H₂ detection. Thermodynamic equilibrium calculations were performed, the description can be found in SI.

3. Results and discussion

3.1. Catalytic tests

The catalytic response in the 175–300 °C temperature range (30 bar, H₂/CO₂ = 3, 16,800 mL/g_{cat}h) displayed in [Fig. 1](#) evidence that in Pd-In₂O₃-Al₂O₃ systems, the methanol synthesis performance of the individual components, Pd-Al₂O₃ and In₂O₃-Al₂O₃, is boosted. In₂O₃ loading plays an important role in performance improvement. The Pd-12In₂O₃-Al₂O₃ catalyst reaches the highest STY values, although these are lower than for Pd-In₂O₃. Significantly, the activity in the RWGS of Pd in Pd-Al₂O₃ [35,36] is largely suppressed when supported on In₂O₃-Al₂O₃. However, to keep a high methanol selectivity above 200 °C, 12 and 23 wt% In₂O₃ loadings are required. The low In₂O₃ loaded Pd-6In₂O₃-Al₂O₃ catalyst, despite reaching CO₂ conversions like Pd-12In₂O₃-Al₂O₃ (and higher than Pd-23In₂O₃-Al₂O₃) is less prone to selectively produce CH₃OH. It is noteworthy that DME is detected in traces (<0.1 % v/v) only beyond 275 °C for the Pd-6In₂O₃-Al₂O₃ sample due to acidic sites on the Al₂O₃ support [37]. The two ternary catalysts, Pd-12In₂O₃-Al₂O₃ and Pd-23In₂O₃-Al₂O₃, are more selective than Pd-In₂O₃; however, the comparison is tricky due to the trade-off between conversion and selectivity. A commercial-like Cu-ZnO-Al₂O₃ catalyst with a high active phase loading (ca. 50 Cu wt.%) achieves higher CO₂ conversion than In₂O₃-based catalysts regardless of the temperature ([Figure S1](#)), but it is more selective to the RWGS, e.g., CH₃OH selectivity is only 10 % at 300 °C. Hence, Cu-ZnO-Al₂O₃ reaches higher STY values at 225 and 250 °C, In₂O₃-based catalysts at 300 °C, while at 275 °C similar values are obtained for both types of catalysts.

Notably, the same trend is observed in the performance of the catalysts operating at 40,800 mL/g_{cat}h and H₂/CO₂ = 4 ([Fig. 2a](#)). The STY reaches values of 0.551 and 0.518 g_{CH₃OH}/g_{cat}h for Pd-

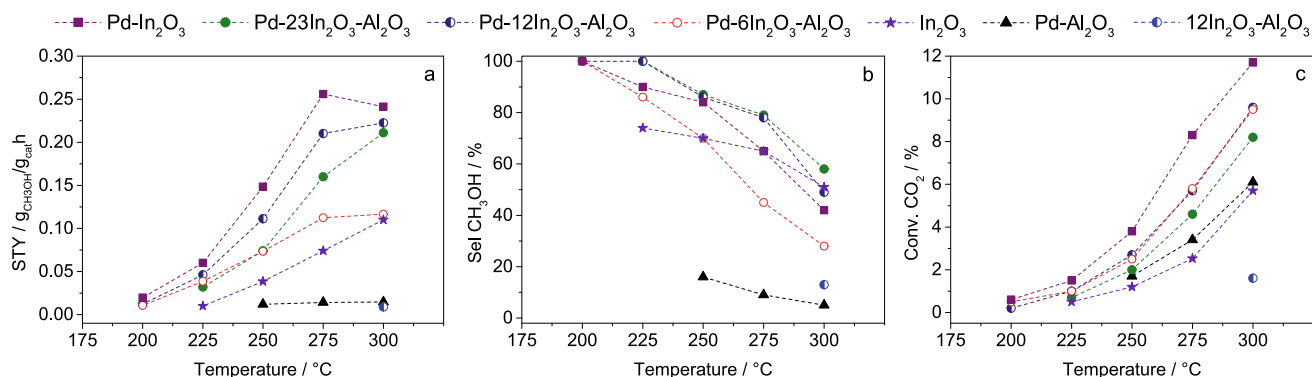


Fig. 1. STY (a), CH₃OH selectivity (b) and CO₂ conversion (c) over Pd-In₂O₃-Al₂O₃ (with different In₂O₃ loading), Pd-In₂O₃, Pd-Al₂O₃, In₂O₃-Al₂O₃ and In₂O₃ catalysts. P = 30 bar, H₂/CO₂ = 3 and 16,800 mL/g_{cat}h. Zero CO₂ conversion points are not reported in the graphs. The cumulative TOS for each catalyst is 8 h. (CH₃OH yields for the different catalysts are reported in [Figure S1](#)).

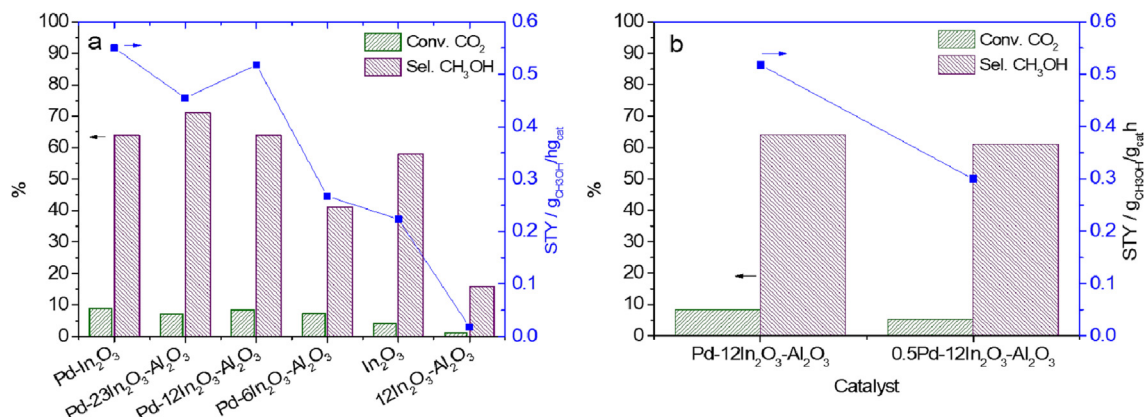


Fig. 2. A) Performance of Pd-In₂O₃-Al₂O₃ (with different In₂O₃ loading), Pd-In₂O₃, In₂O₃ and 12In₂O₃-Al₂O₃ catalysts; b) effect of Pd content on the performance of 12In₂O₃-Al₂O₃ catalysts. P = 30 bar, T = 300 °C, H₂/CO₂ = 4 and 40,800 mL/g_{cat} h. The tests are performed after 8 h of TOS at increasing temperature (175–300 °C).

In₂O₃ and Pd-12In₂O₃-Al₂O₃ respectively. The increase in the CH₃-OH selectivity is likely related to the suppression of the RWGS [38] or the CH₃OH decomposition [39]. Decreasing the Pd content to 0.5 wt% in 0.5Pd-12In₂O₃-Al₂O₃ the STY is nearly halved (Fig. 2b), mainly related to a lower conversion since the CH₃OH selectivity is hardly altered. By expressing the STY values as a function of the different In₂O₃ contents in the Pd-In₂O₃-Al₂O₃ systems (Table S1), it is possible to note that the In₂O₃ intrinsic activity increases as its concentration is lowered (1.98 vs 4.32 g_{CH₃OH}/g_{In₂O₃}h when In₂O₃ passes from 23 to 12 wt%). This behavior is less marked when In₂O₃ is below 12 wt%, suggesting how a proper Pd-In₂O₃ interaction degree (and dispersion) is key for CH₃OH formation.

The effect of the In₂O₃ content on the selectivity is also confirmed for Pd-free In₂O₃-Al₂O₃ samples (Figure S2), though the catalysts activate CO₂ only at 300 °C. It is generally considered that In₂O₃-Al₂O₃ is rather inactive in the CH₃OH synthesis from CO₂, producing mainly CO via RWGS [27,32]. To evaluate whether the low In₂O₃ content or the inclusion of In₂O₃ in the mixed oxide is responsible for activity suppression, a test is performed by loading 0.06 g of pristine In₂O₃ (the same In₂O₃ amount present in 12In₂O₃-Al₂O₃), diluted in SiC (Figure S2). Pristine In₂O₃ is already active at 250 °C and, more significantly, it achieves high CH₃OH selectivity. To discard the role of the preparation method on the poor activity of In₂O₃-Al₂O₃, e.g. embedment of In₂O₃ in the bulk of the catalyst, In is impregnated on Al₂O₃. Similar performances are obtained at 300 °C for both coprecipitated (0.009 g_{CH₃OH}/g_{cat}h) and impregnated (0.011 g_{CH₃OH}/g_{cat}h) materials (Table S2). Hence, the dispersion of In₂O₃ on Al₂O₃ or its interaction likely deteriorates the In₂O₃ catalytic properties.

The catalytic data indicate that Pd is responsible for the increase in CO₂ conversion, while In₂O₃ loading determines the selectivity in CH₃OH. The STY of Pd-12In₂O₃-Al₂O₃ is only 6 % lower than that of Pd-In₂O₃, though in the former the In₂O₃ loading is decreased from 98 to 12 wt% and the catalyst is calcined at a higher temperature (500 °C vs 300 °C) and pre-reduced in H₂/N₂. Indeed, the CO₂ conversion over Pd-In₂O₃ and In₂O₃ drops by ca 40 and 25 %, respectively, when these catalysts are pretreated under the same conditions as the Pd-In₂O₃-Al₂O₃ catalysts (Table S3). This behavior is related to a sintering process (Figure S3a) that decreases the surface area from 124 and 120 m²/g to 78 and 62 m²/g for Pd-In₂O₃ and In₂O₃ respectively and increases the reduction temperature of Pd²⁺ (Figure S3b). All the CO₂ conversions are well below the thermodynamic values (Figure S4), confirming a kinetic regime for both CH₃OH synthesis and RWGS.

The results obtained demonstrate the possibility to attain good performance with a low In₂O₃ loading (i.e. 12 wt%), not previously

achieved in the literature. For instance, when a much higher amount of active metal (Rh 5 or 2.5 wt%) is incorporated on an In₂O₃/Al₂O₃ support [32], the presence of 10 wt% of In₂O₃ leads to a poor CH₃OH yield. Actually, the CH₃OH yield becomes substantial only when the In/Al ratio hits 1/1. Notably, the Pd-12In₂O₃-Al₂O₃ selectivity to CH₃OH at 30 bar is similar to that of a coprecipitated RhIn/Al₂O₃ system operating at 45 bar (270 °C), meaning that the incorporation of 1 wt% of Pd in the In₂O₃-Al₂O₃ is enough to efficiently promote the hydrogenating power of the catalytic system (51.8 g_{MeOH} h⁻¹ g_{Pd}⁻¹). When the results obtained in this work are instead compared with those reported in the literature for Pd-In₂O₃ catalysts that operate at a similar pressure (30 bar), our catalytic results (although with different reaction parameters) are in line with those obtained over Pd-In₂O₃ prepared by impregnation [16] and Pd/In₂O₃ with a hollow In₂O₃ structure [26] (Table S4), despite decreasing the In₂O₃ loading from 98 to 12 wt%. The activity in those works is related to different types of active sites. In the former [16], PdIn is formed in the region between Pd NPs and In₂O₃ support, while in the latter a strong metal-support interaction (SMSI) between Pd and In₂O₃ keeps a high Pd²⁺ species molar fraction [26]. It is noteworthy that by supporting In₂O₃, its intrinsic activity remarkably increases as demonstrated by the STY values calculated on the mass of In₂O₃ for the different catalysts (g_{MeOH} h⁻¹ g_{In₂O₃}⁻¹). Moreover, the effect of the particle size is reported by Frei et al. to explain the differences in the activity of impregnated and coprecipitated catalysts [17]. In impregnated samples with a higher Pd particle size, the activity is a combination of RWGS on large Pd particles and CH₃OH synthesis on In₂O₃. To correlate the catalytic activity of the Pd-In₂O₃-Al₂O₃ catalysts here developed, a deep characterization of their properties during the catalyst lifetime is performed.

3.2. Characterization of fresh and spent catalysts

The structure and specific surface areas of the Pd-containing catalysts resembles those of the respective type of support (In₂O₃ or In₂O₃-Al₂O₃) (Fig. 3a, Table 1, Figure S3c, Table S5). Pd-In₂O₃ contains the cubic In₂O₃ phase. The surface area around 124 m²/g in the fresh Pd-In₂O₃ catalyst drops to 18 m²/g (Table 1) after catalytic performance testing due to sintering, as confirmed by the increase of the mean crystallite size (Figure S5, Table S6). Diffraction patterns of Pd-In₂O₃-Al₂O₃ samples, regardless of the In₂O₃ loading, are characteristic of γ-Al₂O₃. The poor crystallinity of the alumina, with very broad reflections, makes it tricky to obtain any reliable evidence about a possible incorporation of In³⁺ into the γ-Al₂O₃. The broad reflection centered at ca. 30° (2θ) is related to nanosized or amorphous In₂O₃ [40–42]; it partially disappears

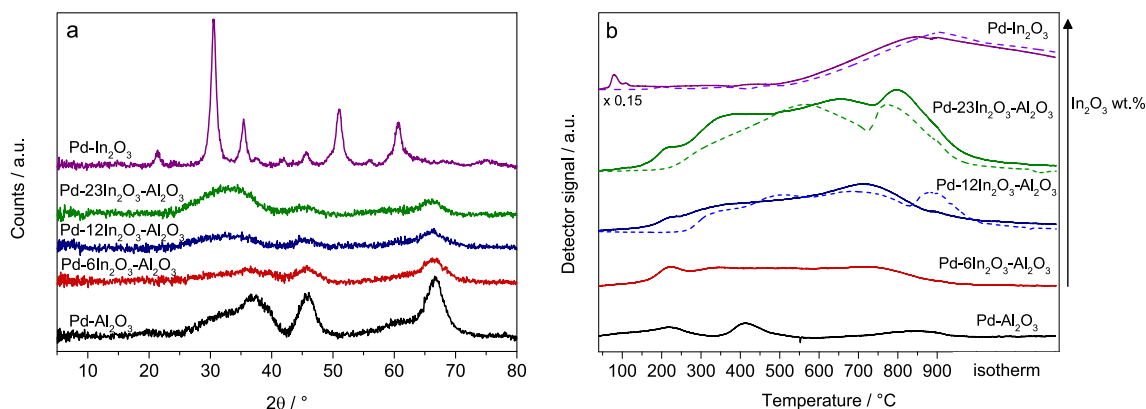


Fig. 3. Characterization of Pd-containing catalysts after calcination: a) XRD patterns; b) H_2 -TPR profiles; dashed lines represent the reduction profiles of oxides in absence of Pd, $12\text{In}_2\text{O}_3\text{-Al}_2\text{O}_3$ (blue), $23\text{In}_2\text{O}_3\text{-Al}_2\text{O}_3$ (green) and In_2O_3 (purple). Note that the H_2 -TPR measurements started at -10°C . (For interpretation of the references to colour in this figure legend, the reader is referred to the web version of this article.)

Table 1

Specific surface area (S_{BET}) values of the catalysts before and after the catalytic assessment and CO chemisorption data of reduced catalysts.

Catalyst	$S_{\text{BET}} / \text{m}^2/\text{g}$		CO chemisorption	
	Calcined	Spent	Pd dispersion / %	CO uptake $\mu\text{mol}/\text{g}_{\text{cat}}$
$\text{Pd-Al}_2\text{O}_3$	216	150	84.5	39.72 ± 1.13
$\text{Pd-12In}_2\text{O}_3\text{-Al}_2\text{O}_3$	260	131	12.9	6.06 ± 0.76
$\text{Pd-23In}_2\text{O}_3\text{-Al}_2\text{O}_3$	210	104	14.4	6.77 ± 0.57
$\text{Pd-In}_2\text{O}_3$	124	18	nd*	nd*

* not detected.

after catalytic testing, which suggests possible re-dispersion and contact with/decoration of Pd nanoparticle species (Figure S5). S_{BET} values of Al_2O_3 supported materials are around $260\text{--}210 \text{ m}^2/\text{g}$, i.e. twice the values of $\text{Pd-In}_2\text{O}_3$. The hydrothermal conditions generated during catalytic tests (high pressure and water production) make it impossible to avoid the sintering of the catalysts; nevertheless, the $\text{In}_2\text{O}_3\text{-Al}_2\text{O}_3$ supported materials retain S_{BET} values above $100 \text{ m}^2/\text{g}$ after the activity testing (ca. 9 h TOS).

The H_2 -TPR profile of In_2O_3 in the mixed oxide follows a more complex reduction path than the pristine oxide, Fig. 3b [40,41]. The typical In_2O_3 reduction profile, with H_2 consumption peaks related to surface (around 200°C) and bulk In_2O_3 (onset at 500°C) [16], transforms into several overlapped peaks spanning 300 to 900°C . Note that the profile of pristine In_2O_3 calcined at 500°C , like $\text{In}_2\text{O}_3\text{-Al}_2\text{O}_3$ samples, only shows a reduction peak above 500°C (Fig. S3b). Hence it could be stated that the incorporation of Al_2O_3 does facilitate the reduction of In_2O_3 , likely forming vacancies or reducing the surface, which could be related to a high dispersion and surface area of In_2O_3 [31]; however, the absence of the low temperature peak suggests that defects in the amorphous In_2O_3 are modified [43]. The high interaction between Pd and the oxide matrix is clearly observed in the profile of $\text{Pd-Al}_2\text{O}_3$. Pd species are reduced in two steps at ca. 220 and ca. 415°C , being related to Pd^{2+} highly dispersed and interacting with the support, respectively. In contrast, Pd^{2+} species reduce at a rather low temperature in $\text{Pd-In}_2\text{O}_3$, shifting the surface In_2O_3 reduction peak towards a lower temperature (ca. 110°C) [17]. In $\text{Pd-In}_2\text{O}_3\text{-Al}_2\text{O}_3$ catalysts, the first Pd^{2+} reduction is clearly identified, however, establishing a relationship between the incorporation of Pd in the In_2O_3 and the reducibility is not straightforward. While in $\text{Pd-12In}_2\text{O}_3\text{-Al}_2\text{O}_3$ Pd promotes the reduction of In_2O_3 by shifting the end of the H_2 uptake at lower temperatures, this behavior is not observed for $\text{Pd-23In}_2\text{O}_3\text{-Al}_2\text{O}_3$. Note that the formation of PdIn intermetallics is reported to happen during TPR [13], the Pd/In

ratio depends on the reduction temperature and for the samples of $\text{Pd-In}_2\text{O}_3\text{-Al}_2\text{O}_3$ it could also depend on the composition.

XPS reveals some changes in the surface of the fresh catalysts depending on the composition (Table 2, Fig. 4). The $\text{In } 3d_{5/2}$ binding energy value in $12\text{In}_2\text{O}_3\text{-Al}_2\text{O}_3$, with and without Pd, is 444.8 eV . This value has been related to the presence of In_2O_3 in similar materials [40,41]; however, it is higher than for $\text{Pd-In}_2\text{O}_3$ (444.0 eV) [16]. Remarkably, the $\text{In } 3d$ peaks are asymmetric, likely due to the presence of other In species such as hydroxides or vacancies/defects in the oxide lattice. The $\text{Al } 2p$ signals of all studied Al-containing catalysts appear at about 74.1 eV , typical of Al^{3+} (Table S7). The $\text{Pd } 3d$ core level spectrum in $\text{Pd-12In}_2\text{O}_3\text{-Al}_2\text{O}_3$ shows a $\text{Pd } 3d_{5/2}$ signal with two contributions at 335.8 and 337.8 eV , which are also recorded in the $\text{Pd } 3d_{5/2}$ signal of $\text{Pd-Al}_2\text{O}_3$. The coprecipitation method followed by calcination at 500°C , provides a high dispersion and interaction of Pd with the Al_2O_3 matrix likely provoking the formation of Pd aluminate responsible for the $\text{Pd } 3d_{5/2}$ signal at high binding energy (338.1 eV) [44]. This strong interaction between Pd^{2+} and the support is not altered in the $\text{In}_2\text{O}_3\text{-Al}_2\text{O}_3$ mixed oxide. Contrarily, $\text{Pd-In}_2\text{O}_3$ only contains one type of Pd species with a BE value for the $\text{Pd } 3d_{5/2}$ signal at 336.5 eV , as previously reported for atomically dispersed Pd^{2+} in In_2O_3 and Pd^{2+} highly interacting with the structure of In_2O_3 nanotubes [26]. The *ex situ* XPS characterization of spent catalysts (Figure S6 and Table 2) only clearly confirms the formation of Pd^0 (335.0 eV) in $\text{Pd-In}_2\text{O}_3$ and $\text{Pd-Al}_2\text{O}_3$. Furthermore, the modification of Pd/In and In/Al ratio values in spent catalysts suggests a decrease in the In surface concentration after the catalytic tests. The decrease in the In surface concentration after reduction and catalytic tests could be related to the growth of In particles or to the formation of some bimetallic PdIn particles that modify the surface composition. Note that a similar Pd/In ratio increase is reported by Araujo et al. [11] The coexistence of Pd^{2+} and the unaltered BE for $\text{In } 3d_{5/2}$ is likely related to the exposure

Table 2

Binding energy (eV) of the core levels (Pd 3d_{5/2} and In 3d_{5/2}) and surface atomic ratios of different catalysts determined from XPS measurements. The values in between brackets are the wt.%.

Catalyst	Treatment	Pd 3d _{5/2}		In 3d _{5/2}		Pd/In	Pd/Al	In/Al
Pd-Al ₂ O ₃	c500	–	335.9 (63)	338.1 (37)	–	–	0.004	–
	reduced	335.1 (71)	–	337.2 (29)	–	–	0.003	–
	spent	335.1 (83)	–	338.0 (17)	–	–	0.003	–
Pd-12In ₂ O ₃ -Al ₂ O ₃	c500	–	335.8 (70)	337.8 (30)	444.8	0.060	0.005	0.082
	reduced	–	335.9 (100)	–	444.7	0.078	0.005	0.067
	spent	–	335.6 (74)	337.5 (26)	444.6	0.080	0.006	0.071
12In ₂ O ₃ -Al ₂ O ₃	c500	–	–	–	444.8	–	–	0.08
	reduced	na*	–	na*	na*	–	–	–
	spent	–	–	–	444.5	–	–	0.07
Pd-In ₂ O ₃	c300	–	336.5 (100)	–	444.0	0.010	–	–
	reduced	335.0 (74)	336.9 (26)	–	443.6	0.020	–	–
	spent	335.2	336.8	–	444.1	0.019	–	–

* not analyzed.

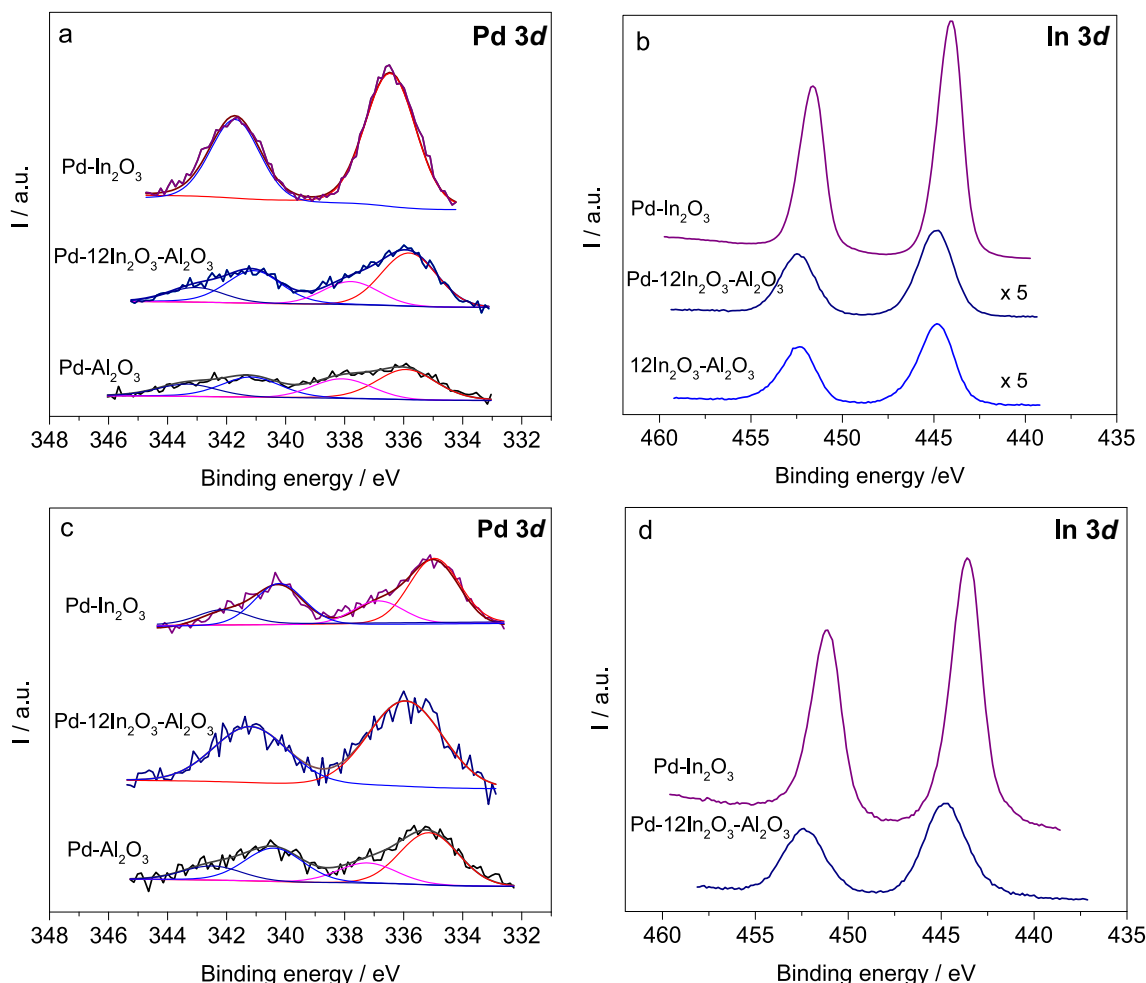


Fig. 4. Pd 3d (a, c) and In 3d (b, d) core level of calcined (a, b) and reduced (c, d) catalysts.

of the samples to the air [45,46], O vacancies could be restored in air [45].

The rising absorption edge in the *ex situ* Pd K-edge XANES spectrum of the spent Pd-12In₂O₃-Al₂O₃ sample matches closely with that of the PdO reference (Figure S7) confirming the Pd particles to be small and liable to (re)oxidation on exposure to air consistent with those data reported for XPS. However, the lower rising absorption edge intensity in combination with a shift towards lower energies seen for the sample post reaction in comparison with a reduced catalyst exposed to the air, suggests some retention

of the metallic state despite the same degree of exposure to atmosphere, which could indicate a possible interaction of Pd and In. A Linear Combination Fitting (LCF) suggests the composition of PdO/Pd metal in the post-reaction sample is split ~ 70:30 % (Table S8). Note however, that the metallic content is too low to extract further EXAFS information on the properties and nature of the metallic component. *Ex situ* EXAFS measurements at In K-edge post reaction (and after reduction) indicate the presence of In₂O₃ lacking long-range order (Figures S7 and S8), which is consistent with the powder diffraction data shown in Fig. 3a and Figure S5 and

could explain the broadness of the In 3d signal in XPS [47]. Note at low k -space values ($2 - 5 \text{ \AA}^{-1}$) of the In K-edge data there is a slight shift due to a decrease in the mean short-range (In-O) distance suggesting a decrease in the extent of In oxidation/differences in In species as also seen in the XPS.

The lack of long-range structure and likely high dispersion of In_2O_3 could be a cause of the drop in the In_2O_3 - Al_2O_3 activity. High In_2O_3 dispersion has been reported to increase CO selectivity in In_2O_3 - ZrO_2 catalysts due to interaction between In oxide and ZrO_2 support [48]. Moreover, the In_2O_3 crystalline phases modify the activity in the RWGS [49]. The disordered oxide structure is described as InO_x polyhedra joined at the corners or edges to form a network structure in which the number of edge-sharing polyhedra is greatly diminished [47], and likely therefore the propensity for vacancy formation. However, the presence of Pd greatly promotes the activity of In_2O_3 dispersed on the Al_2O_3 , which lacks long-range order as evidenced by EXAFS, suggesting a modification on the In_2O_3 by Pd addition. Note that for the active $\text{RhIn}/\text{Al}_2\text{O}_3$ catalyst a crystalline hexagonal In_2O_3 phase is predominant either before and after catalytic tests [32]. The CO_2 -TPD results of reduced catalysts indicate that neither the amount of CO_2 adsorbed, nor the type of basic sites in Al_2O_3 are largely modified after In_2O_3 incorporation (Figure S9). Weak basic sites are mainly present in those catalysts. Conversely, In_2O_3 and Pd- In_2O_3 catalysts contain both weak basic sites and oxygen vacancies [16], which adsorb larger amounts of CO_2 in comparison to the mixed oxide catalysts.

HRTEM and STEM/HAADF of spent catalysts are shown in Fig. 5 and Figures S10–S12. Mesoporous and ill-defined Al_2O_3 support containing Pd- or In-based nanoparticles are observed in Al_2O_3 or In_2O_3 - Al_2O_3 catalysts. Meanwhile round-shaped In_2O_3 nanoparticles with dark spots, which might be related to some sort of porous or defect structure due to the Kirkendall effect (Figure S11b) [50], are clearly identified in the Pd- In_2O_3 catalyst. A mean particle size

of $1.3 \text{ nm} \pm 0.3 \text{ nm}$ is found on the most active spent Pd- $12\text{In}_2\text{O}_3$ - Al_2O_3 catalyst by analyzing HAADF-STEM images of different grains (Fig. 5 a-c). This value corresponds to both Pd and In_2O_3 particles. It is noteworthy that this value is very close to those obtained for Pd- Al_2O_3 ($d \approx 1.8 \pm 0.8 \text{ nm}$) and Pd- $23\text{In}_2\text{O}_3$ - Al_2O_3 ($d \approx 1.5 \pm 0.8 \text{ nm}$), Figure S11. STEM-EELS was chosen to better analyze the composition of the catalysts to achieve a higher degree of localized spectroscopy information than with STEM-EDX. STEM-EELS maps show that Pd is more evenly spread over the Pd- $12\text{In}_2\text{O}_3$ - Al_2O_3 sample where In is more agglomerated. It is not possible to judge if the Pd and In are alloyed from this data; however this supports that the two components are found in close proximity of each other. Additionally, the O intensity is relatively lower where there is a relatively higher intensity of In, indicating a potential reduction of the In (Fig. 5 d-f). The EELS mapping partly damage the sample during acquisition, although this was necessary in order to achieve an adequate signal-to-noise for the maps to be useful (Figure S12).

An estimation of the STY per specific surface area of the indium and palladium species can be obtained by the combination of catalytic activity, XPS and S_{BET} results (Table S9). The performance in terms of CH_3OH productivity over Pd surface remained essentially unchanged whether the support was In_2O_3 or In_2O_3 - Al_2O_3 , meanwhile the intrinsic activity of the indium ca. 10 times higher in the Pd- In_2O_3 - Al_2O_3 system than in the Pd- In_2O_3 catalyst (0.10 vs $0.01 \text{ g}_{\text{CH}_3\text{OH}} / \text{m}_{\text{In}}^2 \text{ h}$).

In summary, a balance between well-dispersed and lack of long-range order In_2O_3 and Pd nanoparticles is required to achieve an enhanced methanol production, likely due to the modification of the vicinity of In_2O_3 and Pd or even the formation of intermetallic compounds. H_2 -TPR suggests that the reducibility or interaction between Pd and In could occur; however, the ease of catalyst reoxidation together with the low Pd loading makes it difficult to

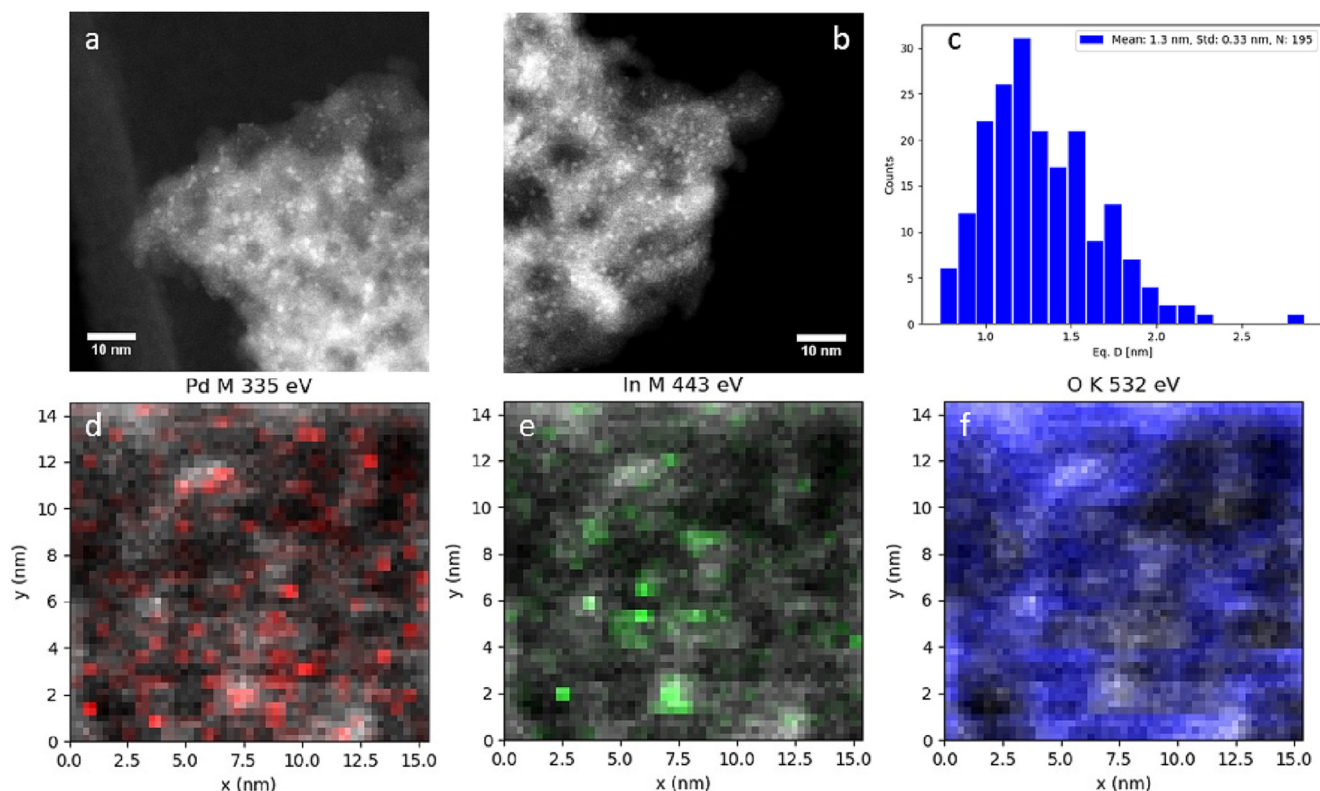


Fig. 5. Spent Pd- $12\text{In}_2\text{O}_3$ - Al_2O_3 imaged with HAADF-STEM (a and b). Based on this the mean average particle size was found to be $1.3 \text{ nm} \pm 0.3 \text{ nm}$ (c). (d-f) STEM-EELS maps of the Pd M, In M and O K edge respectively overlaid on top of the HAADF-STEM acquired at the same time.

obtain any reliable information about these aspects. To further obtain insight into the speciation of the catalysts at the beginning of the reaction, selected catalytic materials were reduced and characterized by CO-chemisorption, XPS and *in situ* XAFS, all measurements performed whilst avoiding contact with air.

3.3. Reduced catalysts

CO chemisorption data, summarized in Table 1, confirm a high Pd dispersion, 84 %, in Pd-Al₂O₃. In contrast, the CO uptake, and in turn the dispersion, largely decreases to ca. 13–14 % for Pd-12In₂O₃-Al₂O₃ and Pd-23In₂O₃-Al₂O₃ catalysts, while it is not possible to measure any CO uptake for Pd-In₂O₃. The drop in CO chemisorption is not related to large Pd particle sizes as previously evidenced by TEM data. Qualitative CO-DRIFTS data spectra provide further insights into the CO-catalyst surface interaction (Fig. 6). In Pd-In₂O₃-Al₂O₃ catalysts, the stretching vibration bands of CO adsorbed in linear (2080 cm⁻¹) and bridge (1930 cm⁻¹) modes are identified [51]. However, in comparison to Pd-Al₂O₃, the former is redshifted, while the latter is smaller and blue shifted. The changes in the CO chemisorption have been previously related to the formation of PdIn intermetallics [52,53] or single Pd sites [17] as well as to the coverage of the surface of Pd (or PdIn) particles by either In⁰ or In₂O₃ [19,54]. Snider et al. based on DFT of PdIn intermetallics established that CO only adsorbs on Pd sites, and the interaction between CO and the surface decreases as the In content increases. Hence the decrease in CO chemisorption in these samples is likely explained to be due to Pd is surrounded by non-CO-adsorbing elements, either In⁰ or In₂O₃.

XPS data of selected reduced catalysts are summarized in Fig. 4 and Table 2. In Pd-In₂O₃ most of the Pd on the surface (74 %) is reduced to Pd⁰ (Pd 3d_{5/2} contribution at 335.0 eV), while the BE of In 3d_{5/2} decreases from 444.0 to 443.6 eV, previously assigned to In⁰ [55] or In_xPd_y intermetallic compounds [39,56]. Remarkably, for reduced Pd-12In₂O₃-Al₂O₃, the In 3d_{5/2} BE (444.7 eV) does not shift towards lower energies, and the Pd⁰ signal at 335.0 eV, clearly identified in reduced Pd-Al₂O₃, is not observed. The only effect of the reduction pretreatment in Pd-12In₂O₃-Al₂O₃ is the disappearance of the peak at 337.8 eV. These results suggest that In₂O₃ is not reduced to In⁰; however, Panafidin et al. found that In₂O₃ and In⁰ clusters located in lattice defects of the support are characterized by similar binding energy values in XPS and thus the respective components strongly overlap [57]. The single Pd 3d_{5/2}

BE at 335.9 eV in the Pd-12In₂O₃-Al₂O₃ reduced catalyst is similar to the one in the calcined sample (and therefore higher than in reduced Pd-In₂O₃ and Pd-Al₂O₃); however, the complete reduction of Pd²⁺ is rather unlikely. The formation of a surface PdIn intermetallic could be inferred taking into account the work by Garcia-Trenco et al. that reported similar Pd 3d_{5/2} (335.9 eV) and In 3d_{5/2} (444.8 eV) BEs for an In depleted PdIn intermetallic coated by In₂O₃ [18].

The Pd-12In₂O₃-Al₂O₃ catalyst was investigated by XANES and EXAFs during *in situ* reduction up to 400 °C. Note that this temperature is 100 °C higher than the reduction temperature to boost the possible PdIn intermetallic formation and In₂O₃ to In⁰ reduction. Initial inspection of the Pd K-edge XANES spectra (Fig. 7a) suggests a shift in oxidation state from Pd(2+) to Pd(0); this is concluded from the observed reduction in rising absorption edge intensity and shift in oscillations to match the metallic Pd standard spectrum. In order to deconvolute these spectra further, LCF was applied to each XANES spectra (Table 3). The Pd species under these conditions do not fully reduce to Pd(0), and there is still a small contribution (~18 %) from oxidic Pd(2+), even after 30 min of reducing gas flow. These results agree with H₂-TPR data and confirm the presence of small Pd species interacting strongly with the support.

The Fourier-transformed EXAFS spectra of the Pd-12In₂O₃-Al₂O₃ catalyst at 400 °C and 400 °C after a 30-min dwell time in Fig. 7c reveal the presence of components at 1.72 and 2.45 Å (phase uncorrected distance), consistent with the presence of both oxidic and metallic Pd. Note the shorter Pd-Pd (2.66 Å) distance seen in the sample when compared to the Pd foil (~2.74 Å) may be due to thermal anisotropy. Fittings of these EXAFS spectra using Artemis (Table 4) reveal that no definitive PdIn alloying could be detected at the beginning or conclusion of the reduction process, where only metallic Pd-Pd(1) and oxidic Pd-O(1) scattering paths could be reasonably fitted. Note that from the Pd-Pd metal coordination number obtained and when accounting for the ~20 % PdO contribution, it is possible to determine the mean Pd nanoparticle size to be ~1.6 nm hence in excellent agreement with the HAADF-STEM data presented above [58]. After the dwell time, a slight contraction of the metallic Pd-Pd(1) bond distance and increase in FT intensity/coordination number suggests the further formation of Pd(0) only species, as opposed to any evidence for Pd-In interaction/alloy formation, where an increase in the mean bond distance would be expected due to the larger atomic radius of In.

The corresponding XANES data for the In K-edge data are given in Fig. 7b with the loss of rising absorption edge intensity consistent with a thermal damping of the In XAFS signal during the reduction treatment. However, there is no obvious change in the phase of the EXAFS oscillations with temperature/time and hence no clear evidence for In₂O₃ reduction or else In-Pd alloying.

The *in situ* reduction of the catalysts allow us to confirm that coprecipitated Pd-In₂O₃-Al₂O₃ catalysts are characterized by a high Pd/oxide matrix interaction that avoids the full Pd²⁺ reduction to Pd⁰ and that is responsible of the nano Pd⁰ particles, regardless of the In₂O₃ loading. Moreover, this strong interaction and the dispersion of lack of long-range nano In₂O₃ may explain the absence of PdIn intermetallics and In⁰ despite the vicinity of the individual elements observed by HAADF/STEM maps, as revealed by the characterization of the bulk of the catalyst by XANES and EXAFS. Though the surface characterization by XPS suggested some kind of Pd-In interaction, likely related to the higher reducibility of surface In₂O₃ indicated also by TPR. Whatever the type of bulk or surface speciation, the Pd and In distributions decrease the CO chemisorption at 35 °C, which could explain the lower CO selectivity of Pd-In₂O₃-Al₂O₃ in comparison to the Pd-Al₂O₃ catalyst. Meanwhile the enhanced activity of the Pd-In₂O₃-Al₂O₃ catalysts is likely related to the close proximity of Pd and In₂O₃, where the

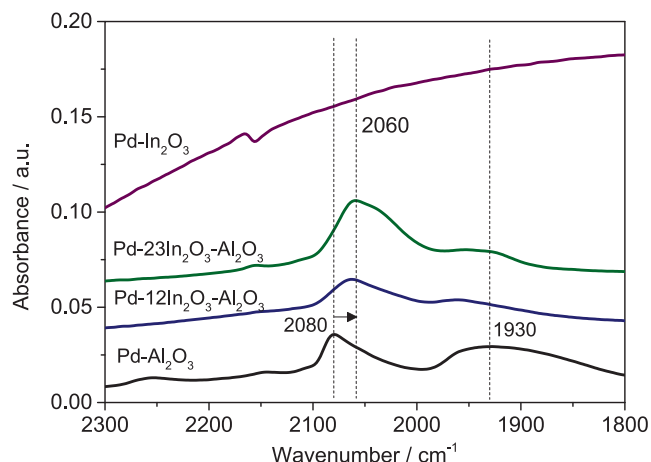


Fig. 6. CO DRIFTS spectra without any processing of Pd-In₂O₃-Al₂O₃ catalysts with 12 and 23 wt% of In₂O₃, and of the Pd-Al₂O₃ and Pd-In₂O₃ counterparts. Pretreatment: reduction at 300 °C (heating rate 2 °C/min) in 2 % H₂/Ar for 2 h and cooled to 35 °C.

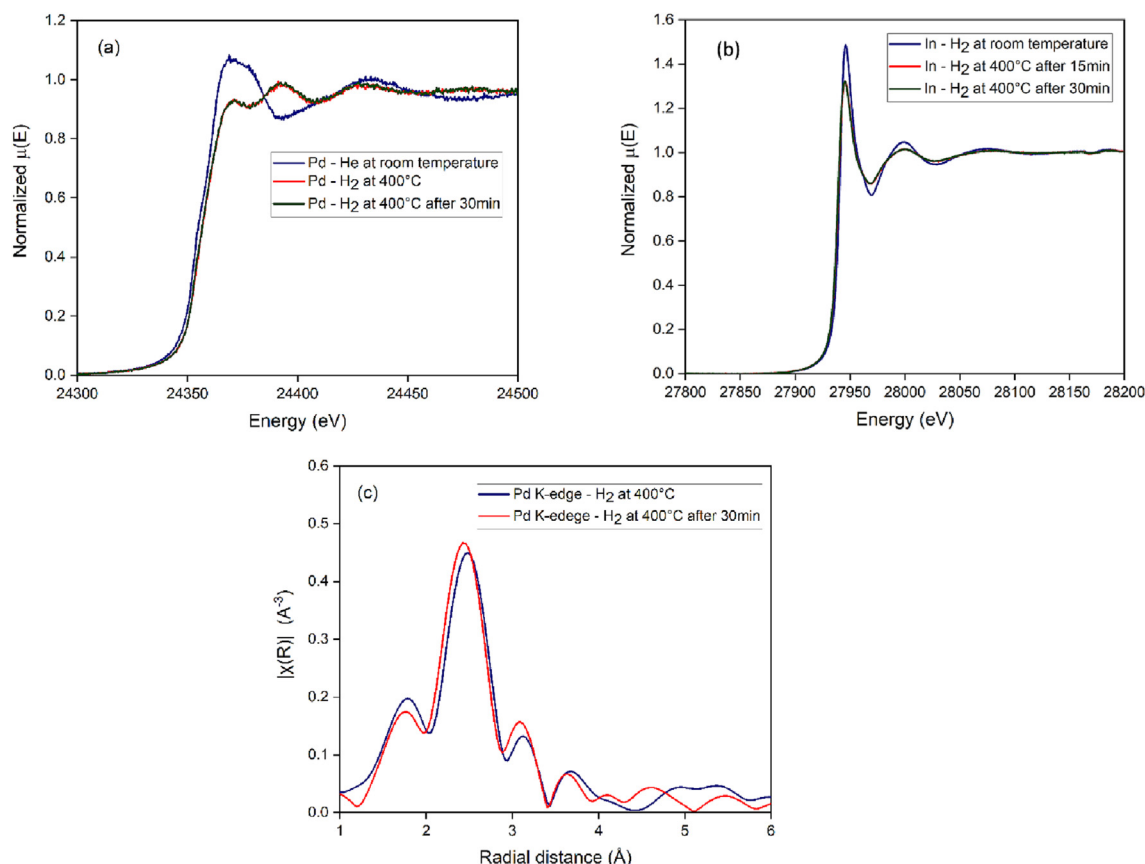


Fig. 7. Pd-12In₂O₃-Al₂O₃: (a) *in situ* XANES spectra at the Pd edge, (b) *in situ* XANES spectra at the In edge, (c) *in situ* R-space plot Pd K-edge. Conditions: i) under He at room temperature; ii) reduction under H₂ at 400 °C; iii) after 15 and/or 30 min under H₂ at 400 °C.

Table 3

Fitting data of the Pd K-edged XANES spectra of Pd-12In₂O₃-Al₂O₃ catalyst at different treatment conditions. Exemplar fitting.

Treatment	R-factor	Chi squared	Met. Pd	Error	Ox. PdO	Error
Room temperature, He	0.00485	0.183	5.4 %	1.6 %	94.3 %	1.6 %
Reduced 400 °C	0.00719	0.247	80.9 %	1.9 %	19.1 %	1.9 %
Reduced 400 °C, 30 min	0.00719	0.248	82.1 %	1.9 %	17.9 %	1.9 %

Table 4

Fit parameters of the *k*²-Weighted EXAFS spectra at the Pd K-Edge.

Treatment	path	R / Å	CN	σ ² / Å ²	E ₀
Reduced 400 °C	metallic Pd-Pd(1)	2.66 ± 0.017	7.08 ± 0.48	0.02 (set)	−3.18
	oxidic Pd-O(1)	2.02 ± 0.039	1.14 ± 0.43	0.03 (set)	−3.18
Reduced 400 °C, 30 min	metallic Pd-Pd(1)	2.63 ± 0.02	7.14 ± 0.63	0.02 (set)	−4.5
	oxidic Pd-O(1)	2.05 ± 0.037	1.83 ± 0.73	0.03 (set)	−4.5

combination of the H₂ splitting ability of Pd with CO₂ activation on In₂O₃ results in enhanced CH₃OH production.

3.4. Stability tests and effect of GHSV and H₂/CO ratio

To further demonstrate the feasibility of dispersing both Pd and In on Al₂O₃ to develop a promising CH₃OH catalyst, the stability of Pd-12In₂O₃-Al₂O₃ was investigated and compared with that of Pd-In₂O₃. Stability tests were performed after the series of tests conducted in the first 8 h of reaction at increasing temperature (175–300 °C) as reported in Fig. 1. The catalyst performances were

then monitored at 280 and 300 °C, feeding a H₂/CO₂ = 4/1 v/v mixture at 40,800 mL g_{cat}^{−1}h^{−1}. Moreover, some control tests were carried out under less favored conditions, i.e. H₂/CO₂ = 3/1, at 16,800 mL g_{cat}^{−1}h^{−1} and 225 °C and 300 °C. Note that the reactor operated under transient conditions, it was shut-down (decreased the temperature and depressurized) in a N₂ flow after every 10 h. Pd-12In₂O₃-Al₂O₃ catalyst is stable for ca. 100 h TOS (Fig. 8a), after that the STY at both 280 and 300 °C decreases by ca. 10 %. These poorer STY values are related to a loss in both conversion and CH₃-OH selectivity at 300 °C, but only to a decrease in conversion at 280 °C (Figure S13). Remarkably the performance at 225 °C is not

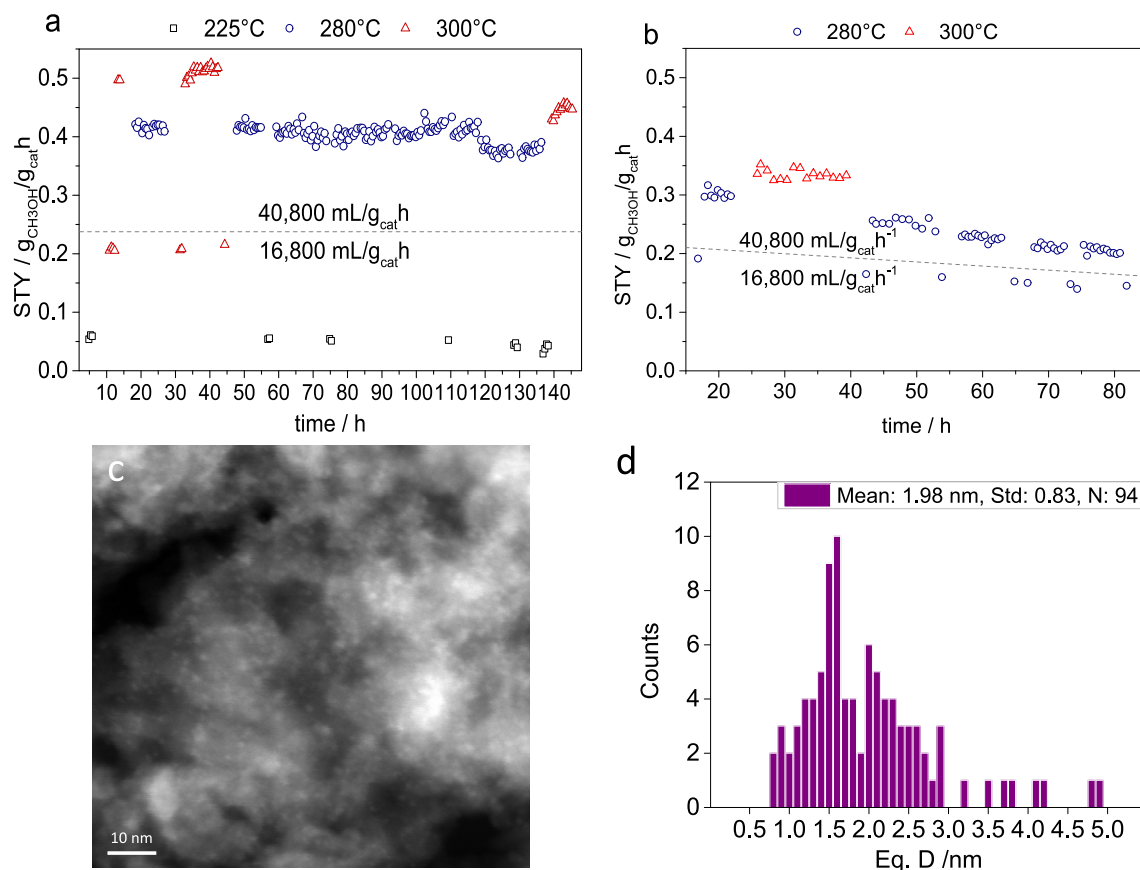


Fig. 8. Evolution of the STY during the stability test over Pd-12In₂O₃-Al₂O₃ (a), Pd-In₂O₃ (b); STEM/HAADF (c) and PSD (d) of the spent catalyst. In figure (a) and (b) the results of the first 8 h of reaction corresponds to the data shown in Fig. 1.

modified with TOS. The Pd-In₂O₃ catalyst is less stable, as evidenced by the poor performance showed after 8 h and the steady decrease in the STY after 40 h TOS (Fig. 8b).

The characterization of the spent catalysts by XRD does not evidence any remarkable change for Pd-12In₂O₃-Al₂O₃, while the Pd-In₂O₃ cubic phase sintered (Figure S14, Table S6). HRTEM images of the Pd-12In₂O₃-Al₂O₃ long term tested catalyst confirm that it is stable with time-on-stream, neither the morphology nor the size of the support and Pd and In₂O₃ particles are largely modified (Fig. 8c, 8d), confirming the role of Al₂O₃ in both dispersing and stabilizing the active centers of the catalyst in the reaction conditions. Only a slight increase in the particle size (from 1.30 ± 0.33 to 1.98 ± 0.83 nm) occurs. A similar particle growth is observed for the long term spent Pd-In₂O₃ which perhaps is consistent with the formation of PdIn particles (Figure S11e). Remarkably, the sintering (crystallite growth) is not accompanied by a particle growth and the pores or defects are still observed as dark spots in HAADF/STEM images (Figure S11e).

Lastly, the effect of the GHSV and the H₂/CO₂ ratio on the performance of Pd-12In₂O₃-Al₂O₃ is investigated at 300 and 280 °C

(Table 5). Regardless of the reaction temperature, and in line with the equilibrium calculations (Figure S4b), the increase of the H₂/CO₂ ratio leads to a better performance, especially in terms of CO₂ conversion, that reaches a value of 10.1 % when the H₂/CO₂ ratio is 5 v/v at 300 °C (STY = 0.6010 g_{CH₃OH}/g_{cat} h). Similarly, CH₃OH selectivity values slightly improve with the increase in the H₂ concentration in the inlet stream (H₂/CO₂ = 5 v/v), hitting 79 % at 280 °C. By increasing the space velocity at 280 °C to 68,000 mL g_{cat}⁻¹h⁻¹ (H₂/CO₂ = 4 v/v), it is possible to boost the CH₃OH productivity to 0.5283 g_{CH₃OH}/g_{cat} h, however under these conditions a decrease in CO₂ conversion (-22 %) and product selectivity (-3 %) is observed.

4. Conclusions

Coprecipitated Pd-In₂O₃-Al₂O₃ catalysts contain highly dispersed Pd²⁺ and In₂O₃ in the Al₂O₃ matrix. The dispersion of In₂O₃ avoids the formation of the crystalline cubic phase and enhances its thermal stability. Moreover, the vacancy formation is likely altered by the lack of long-range order in the dispersed

Table 5

Effect of the temperature, H₂/CO₂ ratio and GHSV on the CO₂ Conversion, Selectivity in CH₃OH and STY of Pd-12In₂O₃-Al₂O₃.

Temperature / °C	H ₂ /CO ₂	GHSV / mL/g _{cat} h	Conv. CO ₂ / %	Sel. CH ₃ OH / %	STY / g _{CH₃OH} /g _{cat} h
300	3	40,800	7.6	59	0.4224
300	4	40,800	8.6	62	0.4969
300	5	40,800	10.1	63	0.6010
280	4	40,800	5.8	77	0.4212
280	5	40,800	6.4	79	0.4814
280	4	68,000	4.5	75	0.5283

In_2O_3 and in turn the activity drops in comparison to pristine In_2O_3 . The incorporation of Pd in the In_2O_3 - Al_2O_3 matrix boosts the activity in methanol synthesis; the role of Pd is likely to favor the H_2 splitting ability of the catalyst, synergistically promoting the CO_2 hydrogenation to CH_3OH over the highly dispersed In_2O_3 particles. The improved activity of the Pd- In_2O_3 - Al_2O_3 catalysts could be related to the close proximity of Pd and In_2O_3 , hence the Pd- In_2O_3 interface could have an important role to the activity, although it was shown that this is primarily dependent on the In_2O_3 loading rather than the Pd particle size. It is possible to achieve similar STY values with a Pd- In_2O_3 - Al_2O_3 catalyst containing only a 12 wt% In_2O_3 than over a Pd- In_2O_3 at 30 bar and $\text{H}_2/\text{CO}_2 = 4/1$ v/v due to an enhancement in the intrinsic activity of In_2O_3 of around seven times (4.32 vs 0.56 g MeOH h^{-1} $\text{g}_{\text{In}_2\text{O}_3}^{-1}$ for Pd- In_2O_3 - Al_2O_3 and Pd- In_2O_3 , respectively). More importantly the performance is stable for 100 h time on stream. The active catalyst can be described as stable Pd^0 and In_2O_3 nanoparticles (both with a dimension of 1.3–1.8 nm) in the Al_2O_3 support, together with some unreduced Pd^{2+} . Even if the formation of a low amount of PdIn surface alloy cannot be excluded, the enhanced interaction between the highly dispersed Pd and In_2O_3 active centers appears to be the predominant factor that affects the catalyst activity.

Although further investigations are needed to better understand the catalytic reaction mechanism and shed light on the complex nanostructure of the catalyst, this work shows that a simple Al_2O_3 support could be used to disperse Pd and In_2O_3 when prepared by coprecipitation, boosting their intrinsic activity and stability in the methanol synthesis, and therefore decreasing its loading. These results could open the way for the development of more economically feasible and stable methanol catalysts based on other types of supports.

Author Contributions

The manuscript was written through contributions of all authors. All authors have given approval to the final version of the manuscript.

Data availability

Data will be made available on request.

Declaration of Competing Interest

The authors declare that they have no known competing financial interests or personal relationships that could have appeared to influence the work reported in this paper.

Acknowledgment

UK Catalysis Hub is kindly thanked for resources and support provided via the membership of the UK Catalysis Hub Consortium and funded by current EPSRC grants: EP/R026939/1 and EP/R026815/1. We thank Dr Martin Wilding, Dr June Callison, and the UK Catalysis Hub BAG access/Diamond Light Source for provision of beam time and support facilities at the beamline B18. This project has received funding from the European Union's Horizon 2020 research and innovation programme under grant agreement No 101022507, project Laurelin. This work was supported by a research grant (9455) from VILLUM FONDEN. E.R.C. Thanks to projects PID2021-126235OB-C32 and TED2021-130756B-C31 of Ministerio de Ciencia e Innovación of Spain and FEDER funds. We thank Elena Rodríguez Aguado for performing the reduction of the catalysts for XPS measurements. Raw data is available on email request to the corresponding authors.

Appendix A. Supplementary data

Supplementary data to this article can be found online at <https://doi.org/10.1016/j.jcat.2023.05.012>.

References

- [1] J. Sehested, *J. Catal.* 371 (2019) 368.
- [2] A. Álvarez, A. Bansode, A. Urakawa, A.V. Bavykina, T.A. Wezendonk, M. Makkee, J. Gascon, F. Kapteijn, *Chem. Rev.* 117 (2017) 9804.
- [3] P. Sharma, J. Sebastian, S. Ghosh, D. Creaser, L. Olsson, *Catal. Sci. Technol.* 11 (2021) 1665.
- [4] J. Wang, G. Zhang, J. Zhu, X. Zhang, F. Ding, A. Zhang, X. Guo, C. Song, *ACS Catal.* 11 (2021) 1406.
- [5] J. Ye, C. Liu, D. Mei, Q. Ge, *ACS Catal.* 3 (2013) 1296.
- [6] W. Wang, Y. Zhang, Z. Wang, J.-M. Yan, Q. Ge, C.-J. Liu, *Catal. Today* 259 (2) (2016) 402.
- [7] K. Sun, Z.J. Fan, J. Ye, J. Yan, Q. Ge, Y. Li, W. He, W. Yang, C.J. Liu, *J. CO₂ Util.* 12 (2015) 1.
- [8] O. Martin, A.J. Martín, C. Mondelli, S. Mitchell, T.F. Segawa, R. Hauert, C. Drouilly, D. Curulla-Ferré, J. Pérez-Ramírez, *Angew. Chem. Int. Ed.* 55 (2016) 6261.
- [9] M.S. Frei, M. Capdevila-Cortada, R. García-Muelas, C. Mondelli, N. López, J.A. Stewart, D. Curulla Ferré, J. Pérez-Ramírez, *J. Catal.* 361 (2018) 313.
- [10] J. Ye, C.-J. Liu, D. Mei, Q. Ge, *J. Catal.* 317 (2014) 44.
- [11] T.P. Araújo, A. Shah, C. Mondelli, J.A. Stewart, D. Curulla Ferré, J. Pérez-Ramírez, *Appl. Catal. B: Env.* 285 (2021).
- [12] H. Lorenz, S. Turner, O.I. Lebedev, G. Van Tendeloo, B. Klötzer, C. Rameshan, K. Pfalter, S. Penner, *Appl. Catal. A* 374 (2010) 180.
- [13] M. Neumann, D. Teschner, A. Knop-Gericke, W. Reschtlowski, M. Armbrüster, *J. Catal.* 340 (2016) 49.
- [14] J.H. Kwak, L. Kovarik, J. Szanyi, *ACS Catal.* 3 (2013) 2094.
- [15] J. Ye, Q. Ge, C.-J. Liu, *Chem. Eng. Sci.* 135 (2015) 193.
- [16] N. Rui, Z. Wang, K. Sun, J. Ye, Q. Ge, C.-J. Liu, *Appl. Catal. B: Env.* 218 (2017) 488.
- [17] M.S. Frei, C. Mondelli, R. García-Muelas, K.S. Kley, B. Puertolas, N. Lopez, O.V. Safonova, J.A. Stewart, D. Curulla Ferré, J. Pérez-Ramírez, *Nat. Commun.* 10 (2019) 3377.
- [18] A. García-Trencó, A. Regoutz, E.R. White, D.J. Payne, M.S.P. Shaffer, C.K. Williams, *Appl. Catal. B: Env.* 220 (2018) 9.
- [19] J.L. Snider, V. Streibel, M.A. Hubert, T.S. Choksi, E. Valle, D.C. Upham, J. Schumann, M.S. Dwyer, A. Gallo, F. Abild-Pedersen, T.F. Jaramillo, *ACS Catal.* 9 (2019) 3399.
- [20] H. Okamoto, *J. Phase Equilib.* 24 (2003) 481.
- [21] Landolt-Börnstein, *Phase Equilibria, Crystallographic and Thermodynamic Data of Binary Alloys*, New Series IV/5G, Springer, Heidelberg, 1997, p. 142.
- [22] Y. Men, G. Kolb, R. Zapf, M. O'Connell, A. Ziogas, *Appl. Catal. A: Gen* 380 (1–2) (2010) 15.
- [23] A. Erdöhelyi, M. Pásztor, F. Solymosi, *J. Catal.* 98 (1986) 166.
- [24] A. Tsoukalou, P.M. Abdala, D. Stoian, X. Huang, M.-G. Willinger, A. Fedorov, C.R. Müller, *J. Am. Chem. Soc.* 141 (2019) 13497.
- [25] A. Cao, Z. Wang, H. Li, J.K. Nørskov, *ACS Catal.* 11 (2021) 1780.
- [26] Z. Cai, J. Dai, W. Li, K.B. Tan, Z. Huang, G. Zhan, J. Huang, Q. Li, *ACS Catal.* 10 (2020) 13275.
- [27] M.S. Frei, C. Mondelli, A. Cesarini, F. Krumeich, R. Hauert, J.A. Stewart, D. Curulla Ferré, J. Pérez-Ramírez, *ACS Catal.* 10 (2020) 1133.
- [28] A. Tsoukalou, P.M. Abdala, A. Armutlulu, E. Willinger, A. Fedorov, C.R. Müller, *ACS Catal.* 10 (2020) 10060.
- [29] C. Yang, C. Pei, R. Luo, S. Liu, Y. Wang, Z. Wang, Z.-J. Zhao, J. Gong, *J. Am. Chem. Soc.* 142 (2020) 19523.
- [30] J.A. Perdigon-Melon, A. Gervasini, A. Auroux, *J. Catal.* 234 (2005) 421.
- [31] M. Chen, J.-L. Wu, Y.-M. Liu, Y. Cao, L. Guo, H.-Y. He, K.-N. Fan, *Appl. Catal. A: Gen.* 407 (2011) 20.
- [32] M. Meng-jung Li, H. Zou, J. Zheng, T.-S. Wu, T.-S. Chan, Y.-L. Soo, X.-P. Wu, X.-Q. Gong, T. Chen, K. Roy, G. Held, S.C.E. Tsang, *Angew. Chem. Int. Ed.* 59 (2020) 16039.
- [33] A.J. Dent, G. Cibin, S. Ramos, S.A. Parry, D. Gianolio, A.D. Smith, S.M. Scott, L. Varandas, S. Patel, M.R. Pearson, L. Hudson, N.A. Krumpa, A.S. Marsch, P.E. Robbins, *J. Phys.: Conf. Ser.* 430 (2013).
- [34] B. Ravel, M. Newville, *J. Synchrotron Radiat.* 12 (2005) 537.
- [35] J. Song, S. Liu, C. Yang, G. Wang, H. Tian, Z.-J. Zhao, R. Mu, J. Gong, *Appl. Catal. B: Env.* 263 (2020).
- [36] X. Wang, H. Shi, J.H. Kwak, J. Szanyi, *ACS Catal.* 5 (2015) 6337.
- [37] E. Lam, J.J. Corral-Pérez, K. Larmier, G. Noh, P. Wolf, A. Comas-Vives, A. Urakawa, C. Copéret, *Angew. Chem. Int. Ed.* 58 (2019) 13989.
- [38] X. Cui, S. Chen, H. Yang, Y. Liu, H. Wang, H. Zhang, Y. Xue, G. Wang, Y. Niu, T. Deng, W. Fan, *Appl. Catal. B: Env.* 298 (2021).
- [39] S. Tada, S. Kayamori, T. Honma, H. Kamei, A. Nariyuki, K. Kon, T. Toyao, K.-I. Shimizu, S. Satokawa, *ACS Catal.* 8 (2018) 7809.
- [40] A. Gervasini, J.A. Perdigon-Melon, C. Guimon, A. Auroux, *J. Phys. Chem. B* 110 (2006) 240.
- [41] M. Chen, J. Xu, Y. Cao, H.-Y. He, K.-N. Fan, J.-H. Zhuang, *J. Catal.* 272 (2010) 101.
- [42] M. Haneda, Y. Kintaichi, N. Bion, H. Hamada, *Appl. Catal. B: Env.* 42 (2003) 57.
- [43] N. Köwitsch, L. Thoni, B. Klemmed, A. Benad, P. Paciok, M. Heggen, I. Köwitsch, M. Mehning, A. Eychmüller, M. Armbrüster, *ACS Catal.* 11 (2021) 304.

- [44] A.S. Ivanova, E.M. Slavinskaya, R.V. Gulyaev, V.I. Zaikovskii, O.A. Stonkus, I.G. Danilova, L.M. Plyasova, I.A. Polukhina, A.I. Boronin, *Appl. Catal. B: Env.* 97 (2010) 57.
- [45] F. Bossola, T. Roongcharoen, M. Coduri, C. Evangelisti, F. Somodi, L. Sementa, A. Fortunelli, V. Dal Santo, *Appl. Catal. B: Env.* 297 (2021).
- [46] J. Li, J. Li, X. Liu, J. Chen, P. Tian, S. Dai, M. Zhu, Y.-F. Han, *Appl. Catal. B: Env.* 298 (2021).
- [47] B. Buchholz, Q. Ma, D. Alducin, A. Ponce, M.J. Yacaman, R. Khanal, J.E. Medvedeva, R.P.H. Chang, *Chem. Mater.* 26 (2014) 5401.
- [48] T.-J. Chen, C. Cao, T.-B. Chen, X. Ding, H. Huang, L. Shen, X. Cao, M. Zhu, J. Xu, J. Gao, Y.-F. Han, *ACS Catal.* 9 (2019) 8785.
- [49] J. Wang, C.-Y. Liu, T.P. Senftle, J. Zhu, G. Zhang, X. Guo, C. Song, *ACS Catal.* 10 (2020) 3264.
- [50] J. Yin, H. Cao, *Inorg. Chem.* 51 (2012) 6529.
- [51] I.V. Yudanov, R. Sahnoun, K.M. Neyman, N. Rösch, J. Hoffmann, S. Schauermaun, V. Johánek, H. Unterhalt, G. Rupprechter, J. Libuda, H.-J. Freund, *J. Phys. Chem. B* 107 (2003) 255.
- [52] J. Jeon, K.-I. Kon, T. Toyao, K.-I. Shimizu, S. Furukawa, *Chem. Sci.* 10 (2019) 4148.
- [53] P.V. Markov, A.V. Bukhtiyarov, I.S. Mashkovsky, N.S. Smirnova, I.P. Prosvirin, Z. S. Vinokurov, M.A. Panafidin, G.N. Baeva, Y.V. Zubavichus, V.I. Bukhtiyarov, A.Y. Stakheev, *Kinet. Catal.* 60 (2019) 842.
- [54] Z. Wu, E.C. Wegener, H.-T. Tseng, J.R. Gallagher, J.W. Harris, R.E. Diaz, Y. Ren, F. H. Ribeiro, J.T. Miller, *Catal. Sci. Technol.* 6 (2016) 6965.
- [55] F.A. Marchesini, S. Irusta, C. Querini, E. Miró, *Appl. Catal. A: Gen.* 348 (2008) 60.
- [56] V.S. Marakatti, S.C. Sarma, S. Sarkar, M. Krajčí, E.M. Gaigneaux, S.C. Peter, A.C.S. *Appl. Mater. Interf.* 11 (2019) 37602.
- [57] M.A. Panafidin, A.V. Bukhtiyarov, I.P. Prosvirin, I.A. Chetyrin, A.Y. Klyushin, A. Knop-Gericke, N.S. Smirnova, P.V. Markov, I.S. Mashkovsky, Y.V. Zubavichus, A. Y. Stakheev, V.I. Bukhtiyarov, *Appl. Surf. Sci.* 571 (2022).
- [58] A.M. Beale, B.M. Weckhuysen, *Phys. Chem. Chem. Phys.* 12 (2010) 5562.